

RADIATIVE MHD SIMULATION OF SUNSPOT STRUCTURE

M. REMPEL¹, M. SCHÜSSLER² AND M. KNÖLKER¹

Draft version October 24, 2018

ABSTRACT

Results of a 3D MHD simulation of a sunspot with a photospheric size of about 20 Mm are presented. The simulation has been carried out with the MURaM code, which includes a realistic equation of state with partial ionization and radiative transfer along many ray directions. The largely relaxed state of the sunspot shows a division in a central dark umbral region with bright dots and a penumbra showing bright filaments of about 2 to 3 Mm length with central dark lanes. By a process similar to the formation of umbral dots, the penumbral filaments result from magneto-convection in the form of upflow plumes, which become elongated by the presence of an inclined magnetic field: the upflow is deflected in the outward direction while the magnetic field is weakened and becomes almost horizontal in the upper part of the plume near the level of optical depth unity. A dark lane forms owing to the piling up of matter near the cusp-shaped top of the rising plume that leads to an upward bulging of the surfaces of constant optical depth. The simulated penumbral structure corresponds well to the observationally inferred interlocking-comb structure of the magnetic field with Evershed outflows along dark-laned filaments with nearly horizontal magnetic field and overturning perpendicular (‘twisting’) motion, which are embedded in a background of stronger and less inclined field. Photospheric spectral lines are formed at the very top and somewhat above the upflow plumes, so that they do not fully sense the strong flow as well as the large field inclination and significant field strength reduction in the upper part of the plume structures.

Subject headings: MHD – convection – radiative transfer – sunspots

1. INTRODUCTION

The physical understanding of sunspot structure has been hampered for decades by 1) insufficient resolution of the fine structure by observations, 2) lack of information about the layers below the visible surface, and 3) insufficient computational power to perform ab-initio 3D MHD simulation of a full sunspot including the surrounding granulation. Recently, we have seen considerable progress on all three of these fronts: 1) adaptive optics, image selection and reconstruction at ground-based telescopes and the advent of spectropolarimetry in the visible from space with the *Hinode* satellite have led to a wealth of new information about the fine structure of sunspot umbrae and penumbrae (e.g. Bharti et al. 2007; Langhans et al. 2007; Ichimoto et al. 2007; Riethmüller et al. 2008; Rimmele & Marino 2006) 2) local helioseismology has started to probe the sub-surface structure of sunspots (e.g., Cameron et al. 2008), and 3) the ever-increasing computational power of parallel computers have made ab-initio simulations of full sunspots come into reach.

While Cameron et al. (2007) simulated solar pores of up to about 3 Mm diameter and did not find indications for the development of a penumbral structure, the first attempt to simulate a sunspot together with the surrounding granulation is due to Heinemann et al. (2007). They considered a rectangular section of a (slab-like) small sunspot of about 4 Mm diameter. The main result of this simulation is the formation of filamentary struc-

tures in the outer part of the spot, various properties of which (such as dark cores, outflows, and strongly inclined magnetic field) are consistent with observational results. However, the filaments found by Heinemann et al. (2007) are much shorter than the typical lengths of real penumbral filaments and the overall extension of the simulated penumbra is very small.

Here we report about results of a sunspot simulation with the *MURaM* code (Vögler et al. 2005). The simulated sunspot has a total diameter of about 20 Mm, shared about equally by umbra and penumbra.

2. SIMULATION SETUP

The primary numerical challenges of performing a large-scale sunspot simulation including umbra, penumbra and granulation are the significant variations of $\beta = 8\pi p/B^2$ and Alfvén velocity encountered at a given geometrical height. While a very low value of β primarily imposes stability problems, very high Alfvén velocities of more than 1000 km·s⁻¹ above the umbra of a spot lead to unacceptably small time steps for an explicit code. In order to cope with these problems, we have modified the *MURaM* code as outlined in Appendix A.

The basic concept of our simulation is similar to that of Heinemann et al. (2007): we consider a slender rectangular section of a sunspot. However, our computational domain is considerably wider and deeper than theirs, permitting us to simulate a much larger sunspot. The rectangular box spans 36.864 Mm × 4.608 Mm in the horizontal (x, y) directions and 6.144 Mm in the vertical (z) direction. The side boundaries are periodic. The top boundary is closed for the flow and the magnetic field is matched to a potential field above. At the bottom, the boundary is open for the flow and the magnetic field kept vertical (for details, see Vögler et al. 2005). In regions of

Electronic address: rempel@hao.ucar.edu

¹ High Altitude Observatory, NCAR, P.O. Box 3000, Boulder, Colorado 80307, USA

² Max-Planck-Institut für Sonnensystemforschung, Max-Planck-Str. 2, 37191 Katlenburg-Lindau, Germany

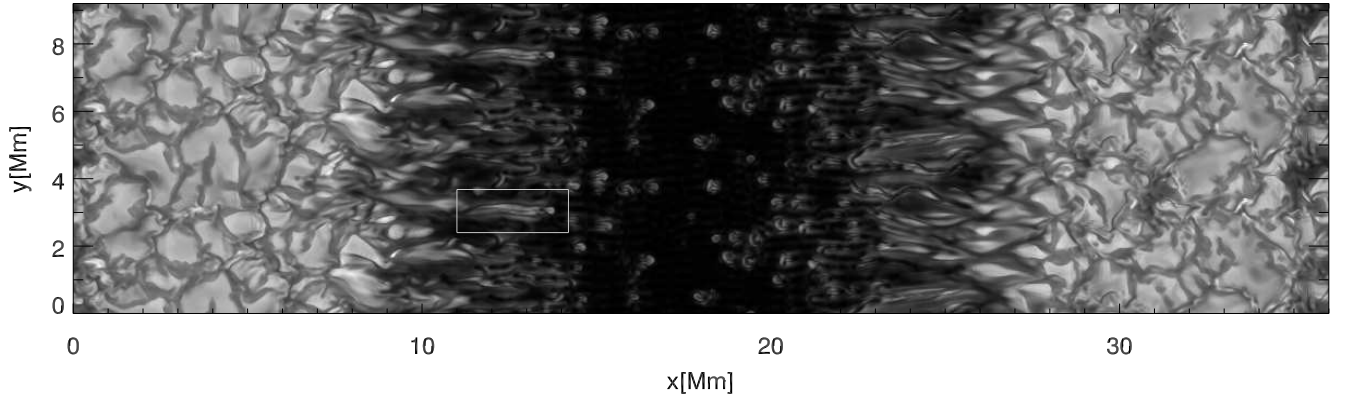


FIG. 1.— Continuum intensity image at 630 nm of the simulated sunspot and its environment (doubled in the y -direction). The bright umbral dots and penumbral filaments have peak intensities between 40% and 90% of the average value outside the spot. The penumbral filaments reach lengths of 2–3 Mm. The white frame indicates the filament studied in detail in Sec. 3.2.

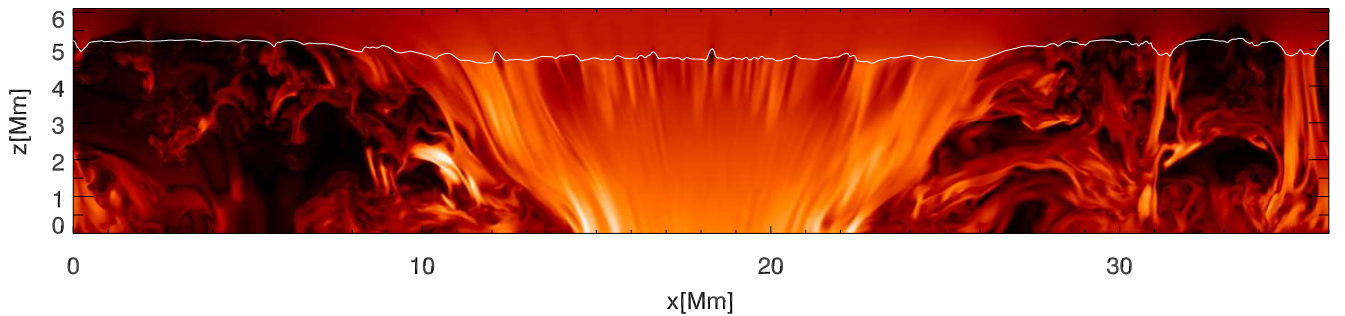


FIG. 2.— Vertical structure of the simulated sunspot. Shown is a color coding of the square root of the field strength on a cut through the simulation in x - z plane at $y = 3.84$ Mm. White color corresponds to the maximum field strength of 9 kG, black to zero field. The whitish line indicates the height of the level $\tau_{630} = 1$. The average Wilson depression of the spot umbra is about 450 km. Separated from the main sunspot, two pore-like structures have formed at $x \approx 31$ Mm and $x \approx 35$ Mm, respectively.

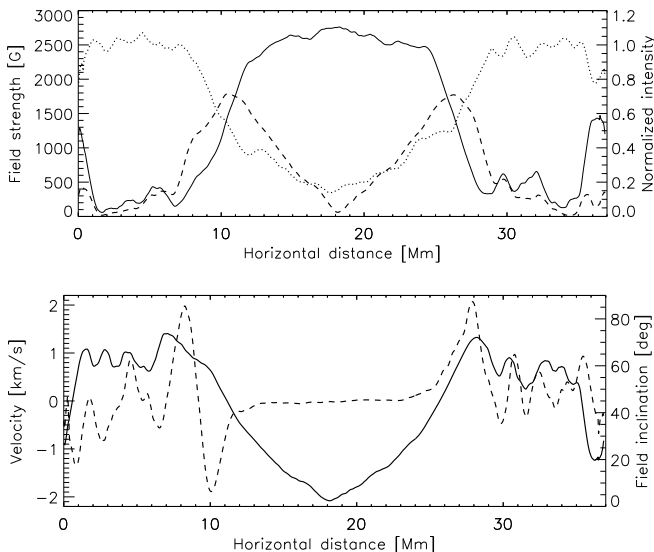


FIG. 3.— Large-scale structure of the simulated sunspot: quantities averaged over the horizontal y -direction as functions of x . *Upper panel:* vertical magnetic field, B_z , at $\tau_{630} = 0.1$ (solid), modulus of the horizontal field component, $|B_x|$, at $\tau_{630} = 0.1$ (dashed), and normalized continuum intensity at 630 nm (dotted). *Lower panel:* magnetic field inclination with respect to the vertical at $\tau_{630} = 0.1$ (solid) and horizontal velocity, v_x , at $\tau_{630} = 1$. (dashed).

strong magnetic field ($B > 1000$ G), the bottom boundary is closed to avoid outflow instabilities in long runs. The radiative transfer is treated in the grey approximation.

The simulation was started from a thermally relaxed non-magnetic run by introducing a 2D (slab) field configuration in the x - z plane with a width of 5 Mm and a strength of 10 kG at the bottom of the box, expanding to 15 Mm at the top. Using a moderate grid resolution of $48 \text{ km} \times 48 \text{ km} \times 32 \text{ km}$ we run the simulation for about 12 hours solar time. After a very dynamic adjustment phase of about 2 hours, elongated filaments with dark cores of about 2 to 3 Mm length started forming in the periphery of the umbra, their heads moving inward. After about 7.5 hours of evolution we restarted from a snapshot and increased the resolution to $32 \text{ km} \times 32 \text{ km} \times 21.33 \text{ km}$.

3. RESULTS

For the detailed analysis of the simulation results, we consider a snapshot taken 30 solar minutes after the start of the high-resolution run. We first present results concerning the global structure of the simulated spot and its average properties and then consider the penumbral filaments.

3.1. Large-scale structure

Fig. 1 presents a continuum intensity image ($\lambda = 630 \text{ nm}$) of the sunspot and its environment. For better visibility, the snapshot has been doubled in y -direction.

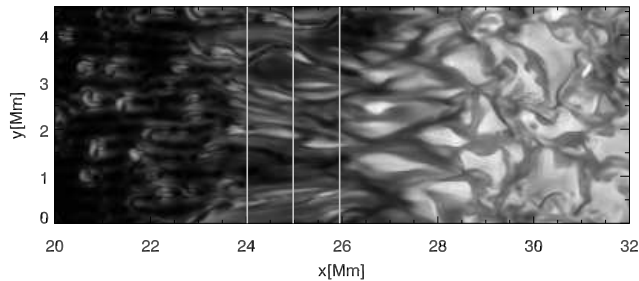


FIG. 4.— Continuum intensity image showing details of penumbral filaments. The vertical lines indicate the positions of the vertical cuts presented in Fig. 5.

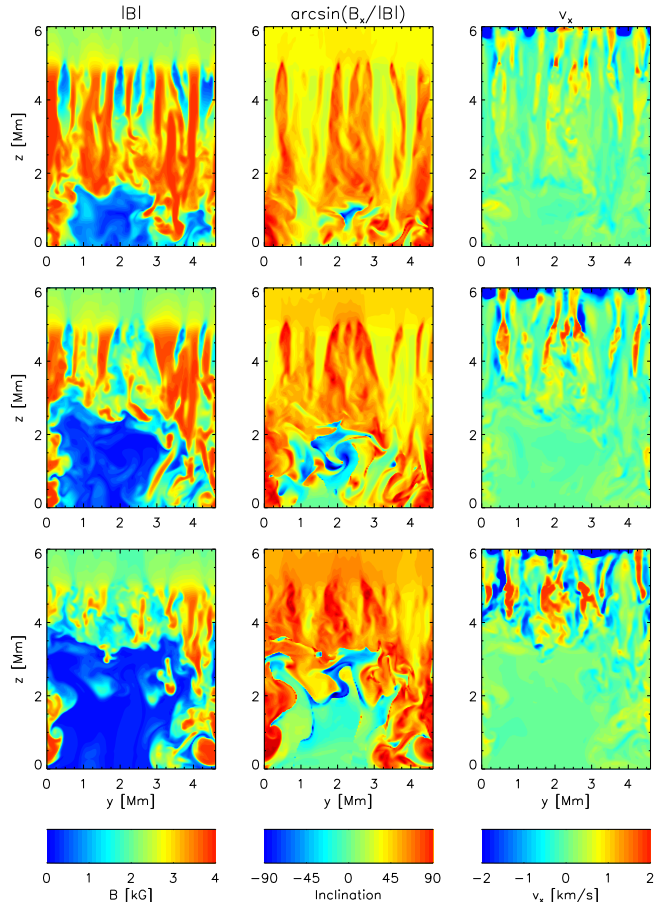


FIG. 5.— Vertical cuts in the y - z plane of magnetic field strength (left), inclination angle (middle) and horizontal velocity (right) for the positions indicated in Fig. 4 (the top row corresponding to the leftmost cut). The magnetic field strength is saturated at 4 kG, the velocity at $2 \text{ km}\cdot\text{s}^{-1}$. The filaments correspond to about 2 Mm deep channels of weaker and almost horizontal field and an outflow of a few $\text{km}\cdot\text{s}^{-1}$.

The spot umbra has a width of about 10 Mm and is surrounded on both sides by a penumbra of about 4 – 5 Mm width, harboring filaments with dark cores. The umbra shows umbral dots similar to those found by Schüssler & Vögler (2006) in a local simulation.

Fig. 2 displays the square root of the magnetic field strength on a vertical cut through the simulation box at $y = 3.84 \text{ Mm}$. The height expansion of the sunspot due to the decreasing gas pressure is well visible. Comparison with Fig. 1 shows that the regions corresponding to

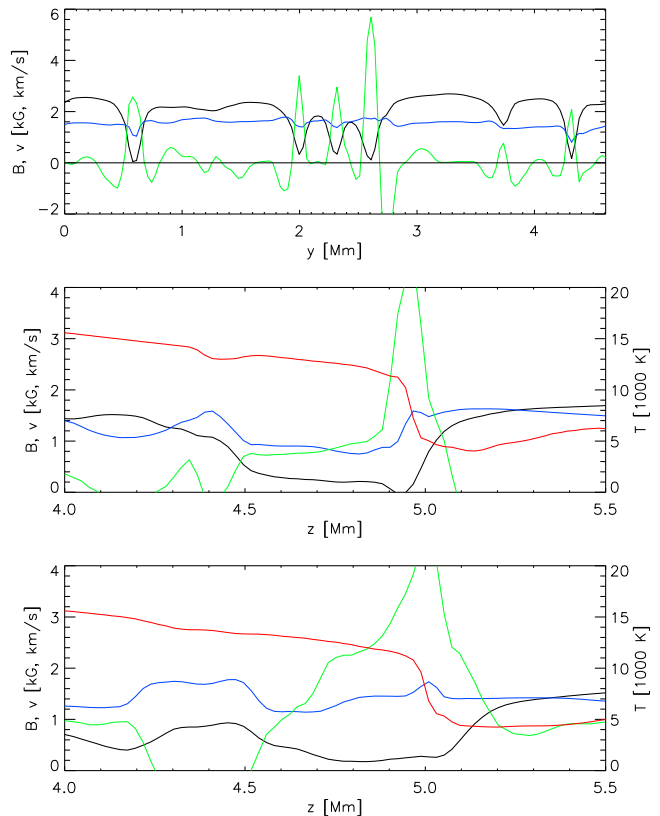


FIG. 6.— Horizontal and vertical profiles of various physical quantities. *Top panel:* Horizontal cut along the middle line in Fig. 4 at height $z = 5 \text{ Mm}$, near the $\tau = 1$ level in the filament. Shown are the vertical field component (B_z , black), the horizontal field component (B_x , blue), and the horizontal velocity component (v_x , green). The vertical field drops to very low values in the filaments, resulting in an almost horizontal field of 1 – 1.5 kG. Along the centers of the filaments, we have an outward directed horizontal flow. *Middle panel:* Vertical profiles of the same quantities through the center of the second filament from the left in the top panel. In addition, the red line shows the temperature profile. The horizontal outflow peaks close to the $\tau = 1$ level, where the magnetic field has the largest inclination. *Bottom panel:* Vertical profiles at the center of the fourth filament from the left in the top panel.

the penumbra (roughly in the ranges $x = 9..14 \text{ Mm}$ and $x = 23..28 \text{ Mm}$) mostly have a deep underlying magnetic structure. In fact, about the same amount of vertical flux emerges in the penumbral part of the simulated spot as in the umbra, so that the penumbra cannot be shallow (cf. Solanki & Schmidt 1993).

Fig. 2 also indicates that the magnetic field is rather inhomogeneous between the level $\tau_{630} = 1$ (indicated by the white line) and about 2 Mm below. This is caused by magneto-convection in the form of upflow plumes which lead to reduced field strength owing to expansion and flux transport by the overturning flow. As we shall discuss further below, the underlying processes for the formation of penumbral filaments are the same as those for the umbral dots (Schüssler & Vögler 2006). Above $\tau_{630} = 1$, the field again becomes rather smooth: owing to the low plasma β in these layers overlying umbra and penumbra, gas pressure gradients cannot maintain strong field inhomogeneities and the field structure has to become almost force-free.

The sunspot has already lost some amount of flux to its environment, which shows a plage-like mean vertical flux

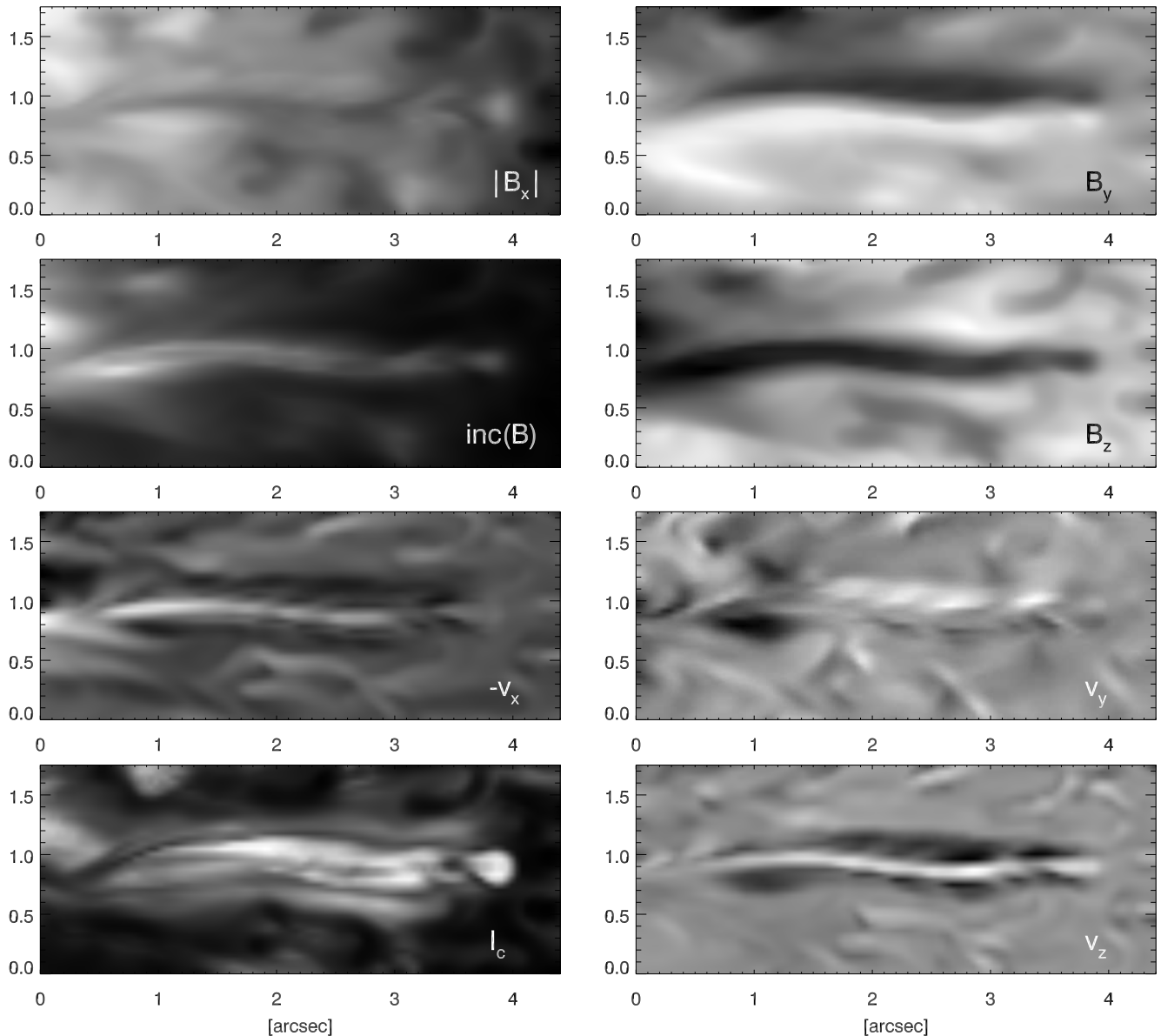


FIG. 7.— Grey-scale maps of physical quantities on the surface $\tau_{630} = 0.1$ for the filament indicated by the rectangular box in Fig. 1. The ranges between minimum (black) and maximum (white) of the various quantities are: $|B_x|$: 670 G ... 1970 G; B_y : -940 G ... 640 G; B_z : 980 G ... 3050 G; B inclination with respect to vertical: 17.5 deg ... 61 deg; $-v_x$: $-1.4 \text{ km}\cdot\text{s}^{-1}$... $3.3 \text{ km}\cdot\text{s}^{-1}$; v_y : $-0.95 \text{ km}\cdot\text{s}^{-1}$... $0.66 \text{ km}\cdot\text{s}^{-1}$; v_z : $-2.1 \text{ km}\cdot\text{s}^{-1}$... $1.5 \text{ km}\cdot\text{s}^{-1}$; I_{630} : 0.13 ... 1.02 of the average value outside the spot.

density of about 200 G at $\tau_{630} = 1$. Most of this flux has been assembled in small-scale flux concentrations in the intergranular lanes (bright structures in Fig. 1), but also pore-like structures have formed, probably supported by the periodic boundary condition.

A more quantitative account of the large-scale structure of the simulated sunspot is provided by Fig. 3, which shows horizontal profiles of average quantities determined in the layers accessible to observation. The profiles of the magnetic field components and its inclination with respect to the vertical agree well with the observational curves determined by Keppens & Martinez Pillet (1996), although the field strength in the simulated penumbra is somewhat high. Average outward horizontal flows with peak velocities of about $2 \text{ km}\cdot\text{s}^{-1}$ are clearly visible in both penumbral regions. The main discrepancy between

the observed and simulated penumbra is the lower mean brightness in the simulation (about 60% of the quiet Sun) compared to the observed value of about 75% (e.g., Schlichenmaier & Solanki 2003). Guided by our experience with umbra simulations, we conjecture that this discrepancy could be due to insufficient thermal relaxation of the magnetic region, so that the magneto-convective processes providing the structuring and the energy transport in the penumbra are still not completely developed.

3.2. Penumbral filaments

Fig. 4 shows an enlargement of the penumbral region on the right-hand side of the continuum intensity map (Fig. 1). The most conspicuous structures are dark-cored filaments of up to a few Mm length. On their end facing the umbra, the filaments typically show bright ‘heads’, which propagate into the umbra. The typical lifetime of

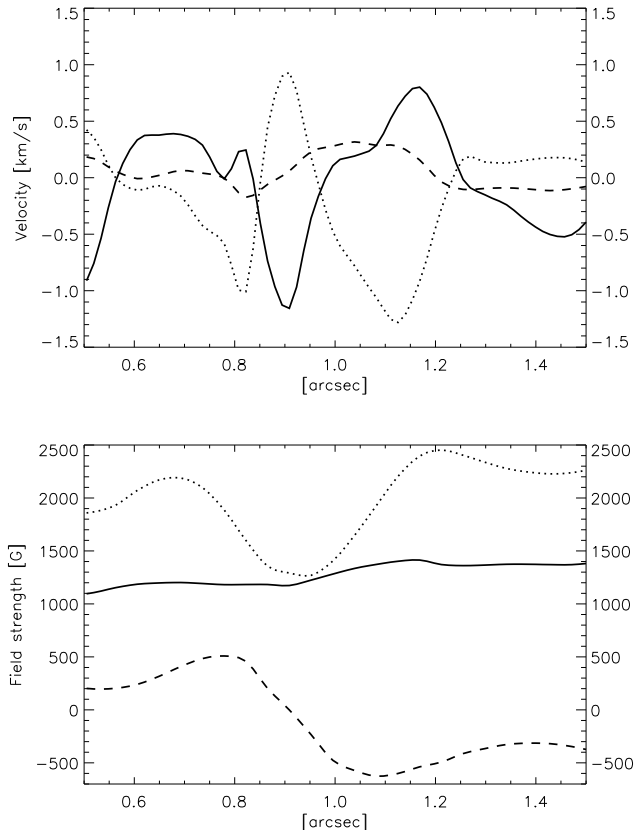


FIG. 8.— Profiles of the magnetic field and velocity components at optical depth $\tau_{630} = 0.1$ along a cut perpendicular to the filament shown in Fig. 7 (cut in y -direction at $x = 2$ arcsec). *Upper panel:* v_x (solid), v_y (dashed), v_z (dotted). *Lower panel:* B_x (solid), B_y (dashed), B_z (dotted).

the filaments is about one hour. The three lines in Fig. 4 indicate the positions of vertical cuts shown in Fig. 5, which give the magnetic field strength, B , the inclination angle with respect to the vertical, $\arcsin(B_x/|B|)$, and the horizontal flow velocity, v_x .

It is obvious from Fig. 5 that the penumbral filaments correspond to slender structures of about 2 Mm depth (near the umbra) and a few hundred km width with significantly reduced overall field strength. The vertical field component, B_z , is reduced to close to zero near the top of the filament, so that an inclination angle of almost 90 deg results, i.e., the field becomes nearly horizontal. In the inner penumbra, the filaments develop within regions of strong magnetic field; only in the periphery of the spot, where the vertical thickness of the penumbra drops to less than 2 Mm, the filaments become more connected to the almost field-free convection zone beneath. Therefore, the filaments in this simulation do not originate from convection penetrating into the penumbra from beneath; they are rather similar to the plume structures leading to umbral dots in the simulation of Schüssler & Vögler (2006), here modified by the presence of a significant horizontal field component.

The third column in Fig. 5 shows that the penumbral filaments are associated with strong horizontal flows away from the umbra. These flows reach their largest velocities of a few $\text{km}\cdot\text{s}^{-1}$ in the upper and outer parts of the filaments, where the magnetic field is most strongly

inclined.

Fig. 6 provides a detailed view of the physical conditions in the filaments by showing horizontal and vertical profiles of magnetic field and velocity components for the cut shown in the middle row of Fig. 5. The horizontal profiles at $z = 5$ Mm in the top panel illustrate the connection between horizontal outflow and almost horizontal magnetic field. The vertical cuts at the positions $y = 1.94$ Mm and $y = 2.6$ Mm, respectively, shown in the middle and bottom panels of Fig. 6 indicate that the outflows are concentrated in the near-surface layers. It is tempting to associate these flows with the Evershed effect (cf. Scharmer et al. 2008).

In what follows, we will study in more detail one prototypical filament (outlined by the white square in Fig. 1). Fig. 7 shows a magnified continuum intensity image at 630 nm (bottom left panel) together with maps of various quantities calculated at the surface $\tau_{630} = 0.1$, roughly corresponding to the layer dominating the spectro-polarimetric information obtainable with the often used neutral iron lines at 630.15 nm and 630.25 nm. This gives a first idea of the actually observable consequences of the physical processes underlying the penumbral filamentation, although definite results will require a detailed comparison with synthetic Stokes profiles from a non-grey simulation, also taking into account image degradation by a realistic point-spread function and noise. Such a study is beyond the scope of this paper.

The intensity image in Fig. 7 shows a bright filament of a few hundred km width, pervaded by a dark lane of about 100 km width. The head of the filament has moved some way into the umbra and has nearly disconnected from the filament, forming a peripheral umbral dot. The maps at constant optical depth $\tau_{630} = 0.1$ show an upflow ($v_z > 0$) of up to $1.5 \text{ km}\cdot\text{s}^{-1}$ at the center of the filament, which is connected to downflows at both sides via outflows in $\pm y$ -direction, perpendicular to the filament axis. In combination with the longitudinal flow along the filament, such a flow pattern is consistent with the recent observations of ‘twisting motions’ in penumbral filaments (Ichimoto et al. 2007; Zakharov et al. 2008). The strong horizontal flow away from the umbra ($-v_x > 0$) along the dark lane is associated with a weaker, laterally more extended, inward return flow at the periphery of the filament. The profiles of the three velocity components along a cut in y -direction through the filament at $x = 2$ arcsec shown in the upper panel of Fig. 8 clearly reveal the flow pattern of a rising plume with laterally overturning motion and a strong longitudinal outflow.

The maps of the magnetic field components in Fig. 7 and the corresponding profiles along the perpendicular cut at $x = 2$ arcsec (lower panel of Fig. 8) show a reduction of the vertical component, B_z , while the component along the filament, B_x , stays almost constant. Accordingly, the field is more strongly inclined and its strength reduced in the filament. The component perpendicular to the filament axis reverses sign at the filament center (above the dark lane), corresponding to the cusp-shaped geometry of the top part of the filament: the strong field sideways of the filament expands and ‘closes’ above the filament. This configuration has recently been confirmed observationally by Borrero et al. (2008).

The structure below the visible filament and its rela-

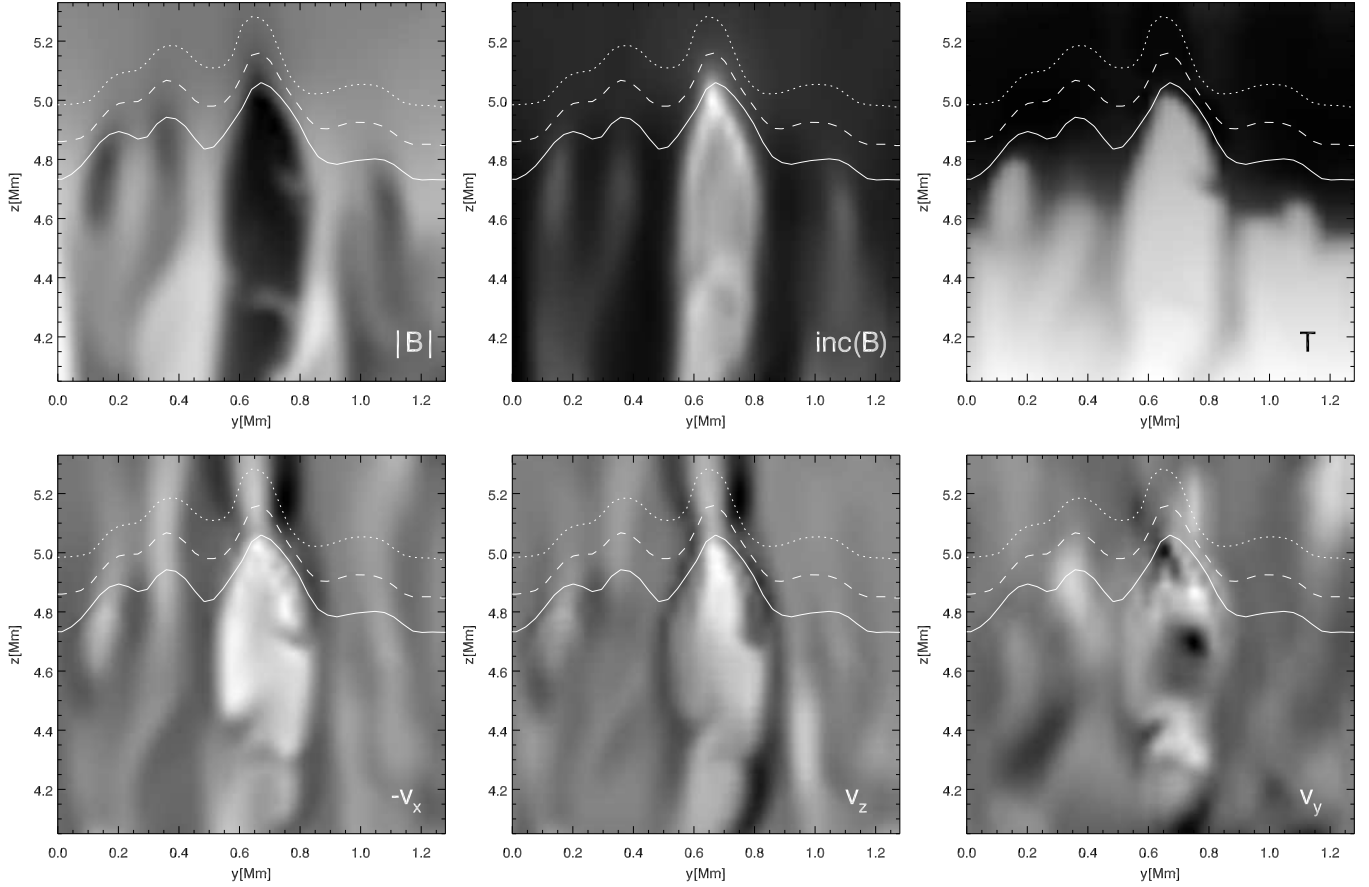


FIG. 9.— Vertical cuts at $x = 2$ arcsec perpendicular through the filament shown in Fig. 7. The vertical scale is the same as used in Figs. 5 and 6, where zero height corresponds to the bottom of the computational domain. The grey-scale ranges between minimum (black) and maximum (white) of the quantities shown are: $|B|$: 480 G ... 4220 G; B inclination with respect to vertical: 20.1 deg ... 90 deg; T : 3890 K ... 15410 K; $-v_x$: $1.88 \text{ km}\cdot\text{s}^{-1}$... $2.09 \text{ km}\cdot\text{s}^{-1}$; v_y : $-0.7 \text{ km}\cdot\text{s}^{-1}$... $0.8 \text{ km}\cdot\text{s}^{-1}$; v_z : $-2.3 \text{ km}\cdot\text{s}^{-1}$... $2.2 \text{ km}\cdot\text{s}^{-1}$. The white lines indicate the levels of $\tau_{630} = 1, 0.1, \text{ and } 0.01$, respectively.

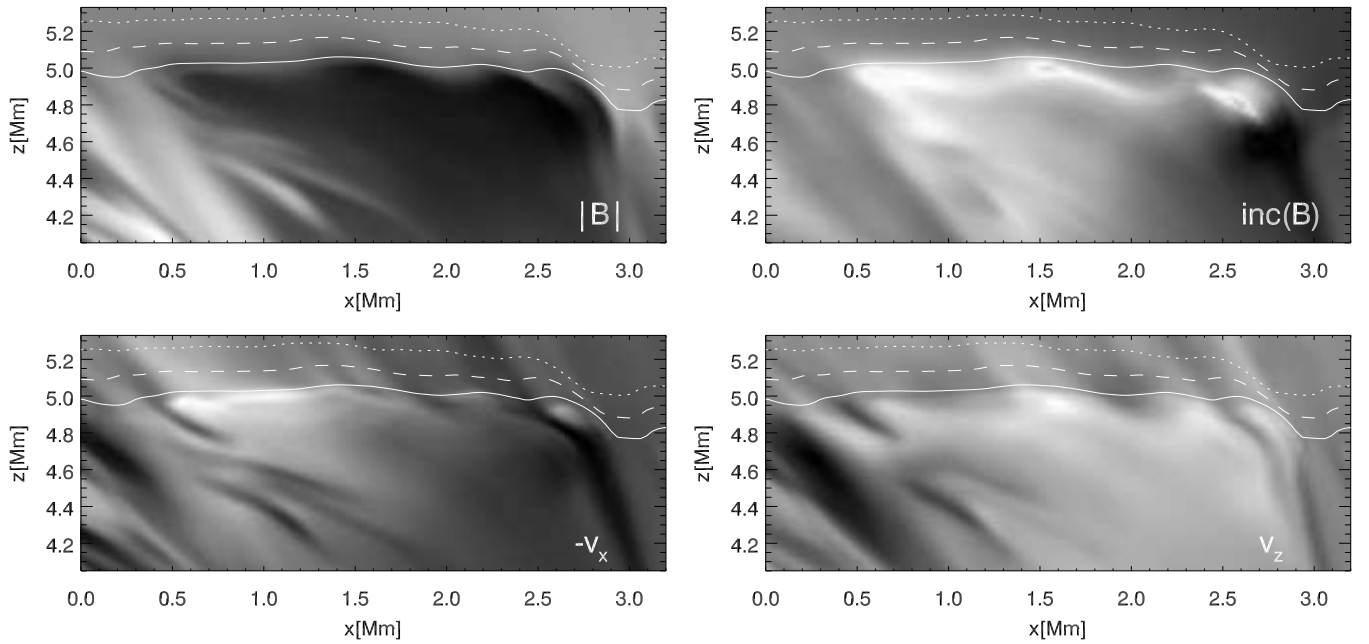


FIG. 10.— Vertical cuts along the center of the filament at constant $y = 0.9$ arcsec in Fig. 7. The grey-scale ranges between minimum (black) and maximum (white) of the quantities shown are: $|B|$: 480 G ... 4220 G; B inclination with respect to vertical: 20.1 deg ... 90 deg; $-v_x$: $-1.3 \text{ km}\cdot\text{s}^{-1}$... $3.6 \text{ km}\cdot\text{s}^{-1}$; v_z : $-2.7 \text{ km}\cdot\text{s}^{-1}$... $2.5 \text{ km}\cdot\text{s}^{-1}$.

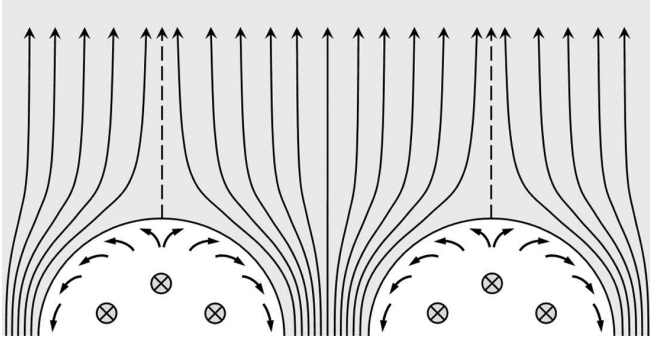


FIG. 11.— Schematic illustration of the basic structure of penumbral filaments as suggested by Zakharov et al. (2008) on the basis of spectro-polarimetric observations. Shown is a vertical cut perpendicular to the filament axes. The bright semicircular areas indicate the uppermost part of the upflow plume, the curved arrows represent the overturning convective flow. Circled crosses indicate the almost horizontal magnetic field and velocity along the filaments. The lines in the grey area are projections of the less inclined magnetic field lines outside the filaments. The intrusion of the plume and flux transport by the overturning motion have pushed aside the less inclined field between the filaments.

tionship to the surfaces of constant optical depth that are relevant for observations are illustrated by vertical cuts perpendicular to and along the filament, which are shown in Figs. 9 and 10, respectively. The perpendicular cuts at $x = 2$ arcsec (Fig. 9) reveal a structure which is very similar to that underlying the umbral dots in the simulations of Schüssler & Vögler (2006): a strong upflow plume in the center with narrow downflows at its sides leads to an elevation of the $\text{iso-}\tau$ surfaces by about 200 km, also clearly visible in the temperature profile. The magnetic field is strongly reduced in the plume since 1) plasma moving upward expands owing to the strong pressure stratification and 2) the overturning horizontal flow transports flux to the downflow regions at the edges of the filament. The latter effect preferentially weakens the vertical field component while horizontal field is replenished by the upflow. The presence of the strongly inclined magnetic field deflects the central upflow outward, leading to a horizontal flow of about $2 \text{ km}\cdot\text{s}^{-1}$ away from the umbra of the spot.

There is some indication that occasionally part of the overturning flow is recirculated into the upflow plume, so that the flow pattern becomes reminiscent to roll convection as originally suggested by Danielson (1961). To see this, consider the velocity components shown in the lower panels of Fig. 9: the central upflow (v_z) drives perpendicular outflows (v_y) near the top of the filament, which feed the downflows adjacent to it. About 300 km deeper, the sign of v_y is reversed, so that we now have a perpendicular inflow, which converges with the central upflow and closes the roll. It is not clear at this moment 1) whether this is a robust or a transient feature of the flow pattern, 2) whether it is really roll-type convection or more related to Kelvin-Helmholtz instability of the downflow, and 3) whether it is realistic at all since the simulation still has a much larger effective magnetic diffusivity than the plasma in a real sunspot. Anyway, its rather small depth extension indicates that such roll convection probably does not contribute much to the convective energy transport, which is mainly provided by the deep upflow plume.

Fig. 10 shows physical quantities on a vertical cut

roughly along the dark lane. It reveals that the structure underlying the visible filament is extended in depth as far as the upflows and the reduction of the field strength are concerned. On the other hand, the horizontal outflow (v_x) and the field inclination sharply peak near optical depth unity and lead to the formation of a narrow, almost horizontal flow channel.

Altogether, the structure of the simulated penumbral filaments may well be represented by the sketch shown in Fig. 11, which illustrates the essence of the high-resolution spectro-polarimetric observations of Zakharov et al. (2008).

A direct connection of the Evershed flow with the basic magneto-convective process in the penumbra has been suggested by Scharmer et al. (2008) on the basis of the simulations of Heinemann et al. (2007). In fact, we find a dominant outward flow due to the deflection of the upward flow in the central part of the filament, which is turned outward by the presence of the inclined magnetic field. The corresponding return flow is mainly located in the regions with less inclined and stronger magnetic field between the filaments (see Figs. 7 and 8); it therefore has a smaller horizontal component at the same (optical) depth. Consequently, the observable average horizontal velocity is outward (see the lower panel of Fig. 3) in accordance with the observed Evershed effect, even though there is no significant overall net outward mass flux in the penumbra. This possibly resolves the long-standing problem of the source and disposal of the mass transported by the Evershed flow (e.g., Solanki et al. 1994). The existence of the weaker inward return flows is a prediction of the simulation that should be testable with high-resolution observations. Note that Ichimoto et al. (2008) have found first indications for flows between the Evershed flow channels. In our current simulation, the penumbral filaments appear to be more separated from each other than shown by observations. While the return flow is clearly visible around separated individual filaments, there are indications that it might be less easily detectable in the case of more densely packed filaments. This needs to be investigated in the future with simulations carried out at higher spatial resolution.

The hot upflow extends over most of the length of the filaments, which provides a rather efficient energy transport to supply the radiative losses of the penumbra. In contrast, the moving-flux-tube model with only localized upflows is far too inefficient to explain the average brightness of the penumbra (Schlichenmaier & Solanki 2003). Similarly, the localized plumes underlying umbral dots can only maintain the much lower brightness of the umbra in comparison with the penumbra, although the basic magneto-convective process is very similar.

The location of the $\text{iso-}\tau$ lines in Figs. 9 and 10 demonstrates that the main part of the upflow plume and the overturning motion underlying the filament is below the visible layers. Spectro-polarimetric observations corresponding to $\tau_{630} \simeq 0.1 \dots 0.01$ just scratch the ‘tip of the iceberg’ and reveal only the uppermost part of the Evershed flow and magnetic cusp structure, which is already laterally much more homogeneous than the underlying main part of the filament. This situation is very similar to that of umbral dot observations and in the past probably has led, together with the effect of insufficient spatial resolution, to ambiguities in the interpretation of

spectroscopic observations of velocity and magnetic field.

4. DISCUSSION

The properties of our simulated sunspot are consistent with the general picture of sunspot structure that has emerged from observational studies. This applies to the overall structure (e.g., distinction between umbra and penumbra, average ‘radial’ profiles of the magnetic field components and inclination angle, average outflow in the penumbra) as well as to the detailed properties of the fine structure of umbra and penumbra. The penumbral filamentation results from magneto-convective energy transport in the form of hot rising plumes, very similar to the process giving rise to umbral dots (Schüssler & Vögler 2006). The inclined magnetic field near the periphery of the spot causes a symmetry breaking which leads to elongated filaments with strong outflows along flow tubes of nearly horizontal field near optical depth unity. In addition to the flow along the filament, the upflow also turns over into a motion perpendicular to the filament axis. Dark lanes appear above the strongest upflows owing to the upward bulging of the surface of optical depth unity and the piling up of plasma in a cusp-shaped region at the top of the filament, above which the less inclined field outside the filament becomes laterally fairly homogeneous. The horizontal outflows are concentrated along the dark lanes. All these properties are consistent with recent observational results (e.g., Bellot Rubio et al. 2005; Rimmele & Marino 2006; Langhans et al. 2007; Ichimoto et al. 2007; Borrero et al. 2008; van Noort & Rouppe van der Voort 2008; Zakharov et al. 2008).

Our results are also consistent with many properties of the short penumbral filaments found by Heinemann et al. (2007), who gave interpretations along very similar lines. The fact that simulations with two rather different numerical codes lead to basically the same picture for the formation of penumbral structure indicates that, in spite of all differences in detail, the simulations have indeed captured essential physical processes. The explanation for the Evershed effect as a natural consequence of rising plumes in an inclined field (cf. Scharmer et al. 2008) connects this flow directly to the basic magneto-convective structure of the penumbra, so that it should occur whenever penumbral structure is present. The geometry of the flow pattern is such that the observable average outflow velocity need not to be connected with a net outflux of mass. This does not exclude the additional presence of siphon flows (e.g., Degenhardt 1993; Montesinos & Thomas 1997; Solanki et al. 1994), but it is much less clear whether the pressure gradients required for a sustained outward siphon flow are maintained always and everywhere in all penumbrae.

What can be said on the basis of our simulation results about the various models that have been proposed to explain the penumbral structure? First of all, we do not see evidence for the ‘moving flux tube’ model and interchange convection (e.g. Schlichenmaier et al. 1998a,b). In our simulations, the progression of the filament heads toward the umbra during their formation phase is not caused by the inward motion of a narrow flux tube, but rather due to the expansion of the sheet-like upflow plumes along the filament.

Furthermore, the simulations combine various aspects

of the ‘embedded flux tube’ model (Solanki & Montavon 1993; Borrero et al. 2005, 2006) and the ‘gappy penumbra’ model (Spruit & Scharmer 2006; Scharmer & Spruit 2006). However, the simulated penumbral filaments are neither intrusions of field-free plasma from below nor are they confined to almost horizontal flux tubes disconnected from their environment, particularly in depth. The uppermost part of the plume structure forming the penumbral filament with its strong horizontal flow and almost horizontal field could possibly be represented by a kind of embedded flux tube. The main feature missing in the embedded flux tube models is the overturning convection within the filament and the deep-reaching upflow of plasma that provides the primary energy supply. In this respect, the underlying plume structure with its reduced (albeit non-vanishing) field strength has much similarity with the ‘gappy’ configuration of the penumbra. This scenario captures the convective origin of the penumbral filamentation, even though the gaps form within the strong magnetic field. As a consequence, the gaps contain a horizontal field and, in most cases, are not connected to the almost field free convecting plasma below the penumbra.

There is no clear evidence in our simulations that the penumbral structure is affected or even caused by the fluting instability as suggested by Weiss et al. (2004). However, the periodic boundary condition in the horizontal (x) direction used in the simulation implicitly corresponds to the existence of identical sunspots just about 20 Mm from the penumbral boundaries, which certainly affects the field structure, particularly the inclination, in the outer penumbra. Therefore, the simulation possibly does not well represent the convective pumping effect suggested by Weiss et al. (2004) as a mechanism for the downward dragging of magnetic flux in the outer penumbra. This might provide a possible explanation for the still rather small extension of the simulated penumbra. Observations in fact indicate that penumbrae are often suppressed on the side of a sunspot which faces a nearby spot of the same polarity.

Altogether, our results indicate a new level of realism in the theoretical modelling of sunspot structure. The properties of the simulated penumbral filaments are consistent with a variety of observational results and provide a basis for a physical understanding of umbral and penumbral structure in terms of magneto-convective processes. On the other hand, there are still clear discrepancies between the numerical results and real sunspots, so that there is some way ahead to be covered towards a completely satisfactory model. Our penumbral structure does not yet appear to be fully evolved and the overall extension of the penumbra is still somewhat small. The average intensity profile indicates that we have simulated the development of an inner penumbra, while the outer penumbra might be more strongly affected by convective pumping (Weiss et al. 2004).

The lower boundary condition remains arbitrary since we still have no reliable observational constraints concerning the subsurface structure of sunspots. Computational limits have forced us to use a rather coarse spatial resolution of 32 km and a fairly small computational box. Furthermore, we could only cover a relatively short overall evolution time. As a consequence, the effective diffusivities in the simulation are still much larger than the

real values. Test calculations with different resolution show that 1) first indications for filamentary structure appear already at a horizontal resolution of 96 km and 2) the reduction of field strength in the plumes increases somewhat when we move to a resolution of 24 km. On that basis, the fundamental physical process of sheet-like plume convection appears to be a robust feature. The results will certainly change in detail (and, hopefully, become even more similar to the observed penumbrae) as resolution increases, but we do not expect totally new processes replacing those that we have described here.

The rapid increase in available computational power and the foreseeable progress in local helioseismology will soon alleviate some of the limitations of the present ap-

proach and thus enable us to carry out even more realistic simulations.

Vasily Zakharov kindly provided Fig. 11. M. Rempel wishes to thank the Institute for Pure and Applied Mathematics (IPAM) of UCLA, Los Angeles for their support to attend the program on ‘Grand Challenge Problems in Computational Astrophysics’, from which this work has benefited significantly. M. Rempel also thanks J. M. Borrero for in-depth discussions regarding observations and models of sunspot structure. The National Center for Atmospheric Research (NCAR) is sponsored by the National Science Foundation.

APPENDIX NUMERICAL SCHEME

To alleviate the time step constraint for an explicit code brought about by high Alfvén velocity, we limit the strength of the Lorentz force in the regions of low β , such that the resulting Alfvén velocity has a given upper bound, c_{\max} :

$$\vec{F}_L = \frac{c_{\max}^2}{\sqrt{c_{\max}^4 + v_A^4}} \vec{J} \times \vec{B}. \quad (\text{A1})$$

Here v_A denotes the value that the Alfvén velocity would have without limitation. The modification of the Lorentz force is applied to regions where $v_A > c_{\max}$ or, in terms of the β value, where

$$\beta < \frac{8\pi p}{\rho c_{\max}^2} \approx \left(\frac{c_{\text{sound}}}{c_{\max}} \right)^2 \approx 0.05. \quad (\text{A2})$$

For the simulations presented in this paper, we have used a value of $c_{\text{sound}} = 7 \text{ km}\cdot\text{s}^{-1}$ to estimate the speed of sound above the sunspot umbra and set $c_{\max} = 31 \text{ km}\cdot\text{s}^{-1}$. Since the magnetic field is already in an almost force free state for $\beta < 0.05$, this correction has only a minor influence on the overall force balance. We have tested this with a 2D run for which we varied the value of c_{\max} by a factor of 3 and found no significant difference. This approach increases the explicit time step limit by about 2 orders of magnitude at zero computational expense, in contrast to the alternative of an implicit treatment of the Lorentz force.

The presence of high and low β regions as well as high and low Mach number flows presents a significant challenge for a numerical scheme to properly resolve all regimes without being too diffusive in any of them. To this end, we have changed the artificial diffusivity scheme of the *MURaM* code. After a piecewise linear reconstruction of the solution, u_i , where the reconstruction slope in each cell Δu_i is limited by an appropriate slope limiter, we use the extrapolated values at the interface $u_l = u_i + 0.5 \Delta u_i$ and $u_r = u_{i+1} - 0.5 \Delta u_{i+1}$ to compute the diffusive flux

$$F_{i+\frac{1}{2}} = \frac{1}{2} c_{i+\frac{1}{2}} \phi(u_r - u_l, u_{i+1} - u_i) (u_r - u_l), \quad (\text{A3})$$

where c denotes the characteristic velocity. Using $\phi = 1$ reduces the scheme to a standard (at least) second order flux (depending on limiter) such as used in a second-order Lax Friedrichs scheme. For the 4th order MHD scheme of the *MURaM* code, we found that a choice of $\phi = \left(\frac{u_r - u_l}{u_{i+1} - u_i} \right)^2$ for $(u_r - u_l) \cdot (u_{i+1} - u_i) > 0$ and $\phi = 0$ otherwise (no artificial steepening) represents the best compromise between maximum stability and minimum diffusion. The diffusivity of the scheme is controlled through the slope limiter, for which we use a linear combination of the most diffusive Minmod and least diffusive Superbee limiter (see, e.g. LeVeque 1990): ε Minmod + $(1 - \varepsilon)$ Superbee and allow ε to vary as function of β (typically 0.5 in high- and less than 0.2 in low- β regions). Furthermore it turned out that it is sufficient to use $c = 0.1 c_{\text{sound}} + v + v_{\text{alf}}$ for the characteristic velocity, which significantly reduces the diffusivity in low Mach number flows. We apply this scheme to all MHD variables and account for effects of (unfortunately unavoidable) mass diffusion in the momentum and energy fluxes. The div \vec{B} error produced by the diffusion scheme is controlled by iterating

$$\frac{\partial \vec{B}}{\partial t} = \mu (\Delta x)^2 \text{grad}(\text{div} \vec{B}). \quad (\text{A4})$$

For values of $\mu = 0.3 \dots 0.5$, typically less than 10 iterations are required to satisfy $\max(\Delta x |\text{div} \vec{B}|) < 10^{-3} B_{\text{rms}}$, which was found to be sufficient. In the results presented in this paper, we did not use any explicit viscosity or magnetic diffusivity. The artificial diffusivities are added once every time step, after completion of the Runge-Kutta loop of the 4th order MHD scheme. The treatment of diffusivity outlined above leads to a scheme that is fully shock-capturing, at least 4th order accurate in smooth regions (higher order is possible depending on slope limiter used), minimally diffusive for low Mach number flows, and stable to β values as low as 10^{-4} .

A very low value of β also leads to problems in codes that use the conservative formulation of the energy equation, since the determination of the internal energy requires to compute the small difference between the nearly equal values of the total and the magnetic energies. To avoid this problem, we switch to an isothermal equation of state in regions where $E_{\text{int}} < 10^{-3}E_{\text{mag}}$ and prevent too small β values by imposing a lower limit for the density when $E_{\text{int}} < 10^{-5}E_{\text{mag}}$. An alternative to this procedure would have been to directly solve an equation for the internal energy at the expense of losing the advantage of the conservative formulation. Since most of the dynamics are driven beneath the photosphere and stability problems only occur in layers with an average density at least 3 orders of magnitude less than the photosphere (and therefore of little dynamical importance), we have preferred to stay with the conservative formulation.

REFERENCES

- Bellot Rubio, L. R., Langhans, K., & Schlichenmaier, R. 2005, *A&A*, 443, L7
- Bharti, L., Jain, R., & Jaaffrey, S. N. A. 2007, *ApJ*, 665, L79
- Borrero, J. M., Lagg, A., Solanki, S. K., & Collados, M. 2005, *A&A*, 436, 333
- Borrero, J. M., Lites, B. W., & Solanki, S. K. 2008, *A&A*, 481, L13
- Borrero, J. M., Solanki, S. K., Lagg, A., Socas-Navarro, H., & Lites, B. 2006, *A&A*, 450, 383
- Cameron, R., Gizon, L., & Duvall, Jr., T. L. 2008, *Sol. Phys.*, 251, 291
- Cameron, R., Schüssler, M., Vögler, A., & Zakharov, V. 2007, *A&A*, 474, 261
- Danielson, R. E. 1961, *ApJ*, 134, 289
- Degenhardt, D. 1993, *A&A*, 277, 235
- Heinemann, T., Nordlund, Å., Scharmer, G. B., & Spruit, H. C. 2007, *ApJ*, 669, 1390
- Ichimoto, K., Suematsu, Y., Tsuneta, S., Katsukawa, Y., Shimizu, T., Shine, R. A., Tarbell, T. D., Title, A. M., Lites, B. W., Kubo, M., & Nagata, S. 2007, *Science*, 318, 1597
- Ichimoto, K., Tsuneta, S., Suematsu, Y., Katsukawa, Y., Shimizu, T., Lites, B. W., Kubo, M., Tarbell, T. D., Shine, R. A., Title, A. M., & Nagata, S. 2008, *A&A*, 481, L9
- Keppens, R. & Martinez Pillet, V. 1996, *A&A*, 316, 229
- Langhans, K., Scharmer, G. B., Kiselman, D., & Löfdahl, M. G. 2007, *A&A*, 464, 763
- LeVeque, R. J. 1990, *Numerical Methods for Conservation Laws* (Basel: Birkhauser-Verlag)
- Montesinos, B. & Thomas, J. H. 1997, *Nature*, 390, 485
- Riethmüller, T. L., Solanki, S. K., & Lagg, A. 2008, *ApJ*, 678, L157
- Rimmele, T. & Marino, J. 2006, *ApJ*, 646, 593
- Scharmer, G. B., Nordlund, Å., & Heinemann, T. 2008, *ApJ*, 677, L149
- Scharmer, G. B. & Spruit, H. C. 2006, *A&A*, 460, 605
- Schlichenmaier, R., Jahn, K., & Schmidt, H. U. 1998a, *ApJ*, 493, L121
- . 1998b, *A&A*, 337, 897
- Schlichenmaier, R. & Solanki, S. K. 2003, *A&A*, 411, 257
- Schüssler, M. & Vögler, A. 2006, *ApJ*, 641, L73
- Solanki, S. K. & Montavon, C. A. P. 1993, *A&A*, 275, 283
- Solanki, S. K., Montavon, C. A. P., & Livingston, W. 1994, *A&A*, 283, 221
- Solanki, S. K. & Schmidt, H. U. 1993, *A&A*, 267, 287
- Spruit, H. C. & Scharmer, G. B. 2006, *A&A*, 447, 343
- van Noort, M. J. & Rouppe van der Voort, L. H. M. 2008, *A&A*, 489, 429
- Vögler, A., Shelyag, S., Schüssler, M., Cattaneo, F., Emonet, T., & Linde, T. 2005, *A&A*, 429, 335
- Weiss, N. O., Thomas, J. H., Brummell, N. H., & Tobias, S. M. 2004, *ApJ*, 600, 1073
- Zakharov, V., Hirzberger, J., Riethmüller, T., Solanki, S., & Kobel, P. 2008, *A&A*, 488, L17